Contents lists available at GrowingScience

Engineering Solid Mechanics

homepage: www.GrowingScience.com/esm

Generalized stiffness of laterally functionally graded materials and implementation to dynamic beam element

Joon Kyu Lee[a], Jong Cheon Lee[b], Jong Min Choi[c] and Byoung Koo Lee[d*]

[a]*Department of Civil Engineering, University of Seoul, Seoul, Korea*
[b]*Department of Smart Construction and Civil Engineering, Donggang University, Gwangju-si, Korea*
[c]*DL E&C, Seoul, Korea*
[d]*Department of Civil and Environmental Engineering, Wonkwang University, Iksan-si, Korea*

A R T I C L E I N F O

Article history:
Received 10 May 2024
Accepted 17 August 2024
Available online
17 August 2024

Keywords:
Generalized stiffness
Laterally-functionally-graded material
Dynamic beam element
Rotary inertia
Free vibration
Mode shape

A B S T R A C T

This study investigates the generalized stiffness of laterally functionally graded materials (LFGMs) and applies these findings to dynamic beam elements. The generalized stiffnesses of LFGM, coupled with material and cross-sectional properties such as flexural and axial rigidity, mass per unit length, and mass-moment of inertia, are explicitly formulated. In the context of LFGM, material properties depend on an asymmetrical power law function with respect to cross-sectional depth. An example of the generalized numerical stiffness of a circular cross-section is provided for various material properties. To illustrate the application of generalized stiffness to dynamic beam elements, free vibration of LFGM beams with rotary inertia is considered. The dimensionless differential equation governing the free vibration of such beams is derived and numerically solved to obtain natural frequencies and corresponding mode shapes. Numerical results demonstrate a good consistency with the finite element method.

Nomenclatures

A = area

A_R = axial rigidity

a_1, a_2 = constant

C_i = ith frequency parameter

D_m = mass density per unit length

d = diameter of circular cross-section

E, E_L, E_U = Young's moduli at any depth, lower and upper sides of cross-section

F_R = flexural rigidity

h_n = neutral axis position

I = second moment of inertia

i = integer mode number, $i = 1,2,3,\cdots$

I_m = mass-density of inertia

* Corresponding author.
E-mail addresses: bkleest@wku.ac.kr (B.K. Lee)

ISSN 2291-8752 (Online) - ISSN 2291-8744 (Print)

doi: 10.5267/j.esm.2024.8.004

$k =$ exponential index

$l =$ beam length

$M_i =$ internal moment

$m =$ modular ratio

$m_1 =$ constant $(= m - 1)$

$s =$ slenderness ratio

$(w, h) =$ Cartesian coordinates for representing circular equation

$(x, v) =$ Cartesian coordinates to depict mode shape

$\alpha =$ neutral axis position ratio

$\Gamma =$ inertia multiplier

$\zeta =$ normalized coordinate $(= h/d)$

$(\xi, \eta) =$ nondimensional Cartesian coordinates

$\rho, \rho_L, \rho_U =$ mass density at any depth, lower and upper sides of cross-section

$\Psi =$ area multiplier

$\omega_i = i$th angular frequency.

1. Introduction

Functionally graded materials (FGMs), conceptualized in Japan in 1984, have seen expanding applications in recent years due to their excellent mechanical characteristics under harsh environmental and thermal conditions. FGMs are currently used in various engineering fields, including architecture, civil engineering, biomedicine, aerospace, and precision mechanical engineering (Zaczynska & Kazmierczyk, 2020). FGMs are typically classified based on the direction of material grading: axially functionally graded materials (AFGMs) and laterally functionally graded materials (LFGMs) (Javania et al., 2019; Czechowski & Kolakowski, 2019). In AFGMs, material properties such as Young's modulus and mass density vary along the axial direction, while properties remain constant laterally across the cross-section. Conversely, in LFGMs, material properties are graded laterally, with axial properties remaining unchanged. This paper primarily focuses on LFGMs (Trinh et al., 2016). Over the past four decades, numerous studies have addressed AFGMs and LFGMs in structural analysis. Key works related to FGMs encompass both AFGM and LFGM, which will be briefly reviewed.

1.1. AFGM Studies

Representative studies in AFGM include those by Alshorbagy et al. (2011), who derived a system of equations for a beam's dynamic properties utilizing the virtual work principle under Euler-Bernoulli beam theory. Horibe and Mori (2015) explored the non-linear response of tapered cantilever bend beams subjected to a transverse point load, while Lee and Lee (2019) investigated the free vibrations of a circular arch based on dynamic equilibrium principles incorporating a second-degree polynomial for material properties. Additional studies by Lee and Lee (2022a) addressed the optimization of buckling loads for columns under various end conditions and volume constraints, and another investigation by Lee and Lee (2022b) focused on out-of-plane free vibration of horizontal curved beams with rectangular and elliptical cross-sections, assuming a quadratic relationship for material properties in the axial direction.

1.2. LFGM Studies

Key research focused on LFGMs includes the work of Qatu and Elsharkawy (1993), who employed the Ritz method to determine accurate natural frequencies of laminate composite arches. Kang and Li (2009) used large deflection theory to analyze the elastica behavior of nonlinear cantilever beams under end forces, while Malekzadeh et al. (2009) studied free vibrations of deep circular arches in a thermal environment based on first-order shear deformation theory, assuming temperature-dependent material properties. Malekzadeh (2009) also analyzed the free vibration of LFGM thick circular arches subjected to thermal prestressing with uniform and variable temperature rises. Other notable studies include those by Yousefi and Rastgoo (2011), Zhao et al. (2012), Raki et al. (2012), Liu and Shu (2014), Sitar et al. (2014), and Huynh et al. (2017), each contributing to the academic discourse surrounding LFGMs.

As summarized, considerable research has focused on various aspects of AFGMs and LFGMs, including grading types, structural member configurations, cross-sectional shapes, modeling approaches, solution methodologies, secondary effects influencing FGM behavior, and foundational support types. Despite the diversity of these topics, existing literature has not explicitly formulated the coupled cross-sectional and mechanical properties of LFGMs, such as axial rigidity A_R, flexural

rigidity F_R, mass per unit length D_m, and mass-moment of inertia I_m.

In structural engineering, physical parameters often result from the product of two distinct parameters. For example, flexural stiffness F_R, defined as the product of the area moment of inertia I and Young's modulus E, can be expressed as $F_R = EI$ (Gere & Timoshenko, 1980), representing a critical quantity in structural analysis.

For AFGMs, F_R is easily determined as $F_R = EI$ for a given cross-section, as E is uniform along the lateral cross-section depth despite variations in the axial direction. In contrast, for LFGMs, expressing F_R as $F_R = EI$ is inappropriate due to the dependence of E on section depth. Therefore, a deterministic explicit expression for LFGM stiffness is required. Additional generalized stiffness quantities, such as A_R, D_m, and I_m, also require consideration.

This study consists of two principal components. First, it formulates the generalized stiffnesses of A_R, F_R, D_m, and I_m for LFGMs. The circular cross-section is chosen for the stiffness formulation. Second, an application example pertains to dynamic beam elements, specifically focusing on bending-related issues in structural mechanics, while the analysis of free vibration of beams serves as an application context. Numerical results for (A_R, F_R, D_m, I_m) are presented in tabular and graphical formats, providing a detailed discussion. The derived ordinary dimensionless differential equation governing free vibration in beams with rotary inertia is also presented. This equation is numerically solved to obtain natural frequencies and mode shapes, with results extensively analyzed.

2. Graduation for material properties in LFGM

Fig. 1(a) illustrates a circular cross-section composed of LFGM, characterized by a diameter d and represented in Cartesian coordinates (w, h). The material properties of mass density ρ and Young's modulus E exhibit an asymmetrical gradient along the vertical coordinate h measured from the origin o. Figure 1(b) displays the asymmetric scale profile of (ρ, E) as a function of h, with the (ρ, E) axis perpendicular to the sectional plane (w, h) shown in Fig. 1(a). The cross-section, when subjected to external loading, is assumed to remain its plane after deformation. Consequently, the strain distribution ε is linear along h as depicted in Fig. 1(c), where h_n marks the neutral axis position, and ε_L signifies the strain at $h = 0$.

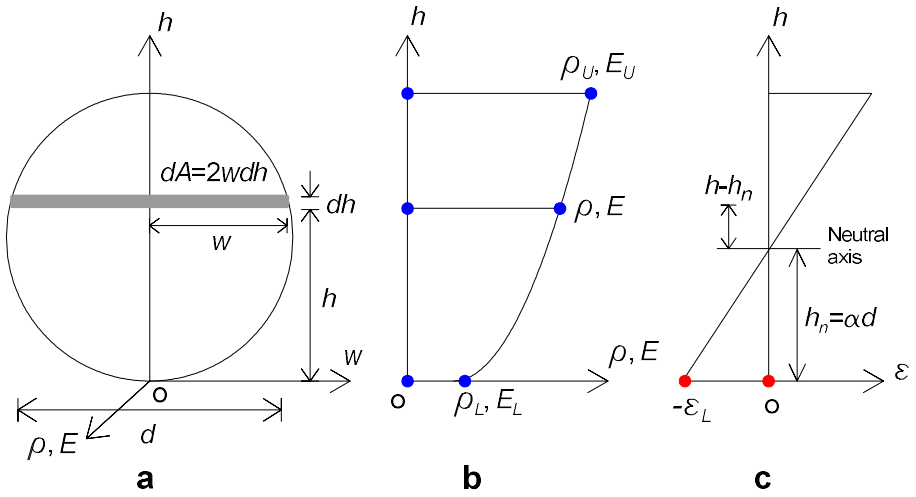

Fig. 1. (a) LFGM circular cross-sections, (b) Asymmetric scaled profile of material properties (ρ, E), and (c) Distribution of strain ε due to bending moment.

The graded function of (ρ, E) shown in **Fig. 1(b)** can be expressed arbitrarily; however, for this study, a power-law function selected from the literature (Akgoz & Civalek, 2013; Noori et al., 2018) is employed:

$$\rho = \rho_L[a_1(h/d)^k + a_2];\ E = E_L[a_1(h/d)^k + a_2] \text{ for } 0 \le h/d \le 1, \tag{1}$$

where k represents a positive exponential index, and ρ_L and E_L denote the mass density and Young's modulus at $h/d = 0$, respectively, with constants a_1 and a_2 determined by given material properties. It is essential to note that the profile illustrated in Eq. (1) is asymmetric concerning the central axis of the circular cross-section, resulting in an unknown position for h_n.

To determine constants a_1 and a_2, the modular ratio m is introduced:

$$m = \frac{\rho_U}{\rho_L} = \frac{\rho_{(h/d)=1}}{\rho_L};\ m = \frac{E_U}{E_L} = \frac{E_{(h/d)=1}}{E_L}, \tag{2}$$

where ρ_U and E_U are the mass density and Young's modulus at $h/d = 1$, respectively. It is assumed that the modulation ratio applies uniformly to both (ρ, E) simultaneously (Akgoz & Civalek, 2013; Noori et al., 2018).

Using the two coordinate points $(0, \rho_L)$ and $(h/d\,, m\rho_L)$ depicted as ● in **Fig. 1(b)**, the constants are defined as a_1 and a_2. Consequently, the functions for (ρ, E) in Eq. (1) simplify to:

$$\rho = \rho_L(m_1\zeta^k + 1);\ E = E_L(m_1\zeta^k + 1) \text{ for } 0 \leq \zeta \leq 1, \tag{3}$$

where $m_1 = m - 1$ and ζ is the normalized coordinate defined as $\zeta = h/d$.

As illustrative examples of scaled profiles as expressed in Eq. (3), Fig. 2 showcases the asymmetric scaled profiles of the dimensionless curves (ρ/ρ_L) and (E/E_L) along h/d for selected values $k = 0.5, 1, 2$ and $m = 0.5, 1, 2$. Profile curves with larger exponent indices k are positioned further from bottom to top at $h/d = 0$, where the profile curve is nonlinear for $k \neq 1$ and linear for $k = 1$, regardless of m. For $m = 1$, the scaled profiles exhibit uniform distribution, i.e., $\rho/\rho_L = 1$ and $E/E_L = 1$, consistent with the characteristics of a conventional homogeneous material cross-section.

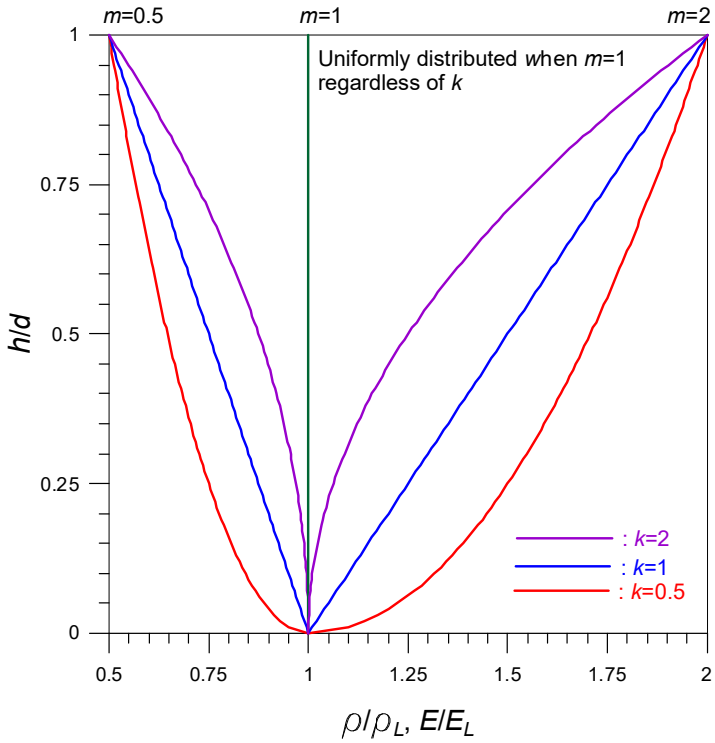

Fig. 2. Examples of scaled profiles of (ρ/ρ_L) and (E/E_L) along h/d for given values of k and m.

3. Generalized stiffness coupled with material and cross-sectional properties of LFGM

3.1. Position of neutral axis of LFGM cross-section

In structural analysis involving bending, identifying the position of the neutral axis is crucial, as this is where the bending strain/stress equals zero. With the rotated cross-section assumed to remain planar after deformation, the distribution of strain ε is linear along h, as illustrated in **Fig. 1(c)**, with the unknown h_n marking the neutral axis's position.

The neutral position ratio α of the LFGM cross-section can be defined as:

$$\alpha = \frac{h_n}{d} \text{ for } 0 < \alpha < 1, \tag{4}$$

where h_n can be expressed as $h_n = \alpha d$.

Given that $\varepsilon = 0$ at $h = h_n$, the linear equation for ε concerning h or the normalized coordinate $\zeta(= h/d)$ with $\varepsilon_L = \varepsilon_{h=0}$ can be derived as:

$$\varepsilon = \varepsilon_L[h/(\alpha d) - 1] = \varepsilon_L(\zeta/\alpha - 1). \tag{5}$$

The resulting bending stress σ at ζ can then be expressed using Hooke's Law:

$$\sigma = E\varepsilon = E\varepsilon_L(\zeta/\alpha - 1), \tag{6}$$

noting that while ε is linear, σ is nonlinear due to the nonlinearity of E.

In Fig. 1(a), the internal moment dM_i generated in the infinitesimal gray shaded area dA by the external bending moment can be expressed as:

$$dM_i = (\sigma dA)|h - h_n|, \tag{7}$$

with $|h - h_n|$ representing the distance between the neutral axis and area dA as indicated in **Fig. 1(c)**.

To satisfy moment equilibrium, the total internal moment M_i across the entire area A must equal zero:

$$M_i = \int dM_i = \int \sigma|h - h_n|dA = 0. \tag{8}$$

The unknown α of the circular cross-section can now be determined. The circular cross-section, with diameter d as shown in Fig. 1(a), is defined by:

$$w^2 + (h - d/2)^2 = (d/2)^2. \tag{9}$$

From Eq. (9), the coordinate w corresponding to dA at h can be expressed as:

$$w = \frac{d}{2}\sqrt{1 - (2h/d - 1)^2}. \tag{10}$$

The area dA at height h is defined using the normalized coordinate $\zeta(= h/d)$:

$$dA = (2w)dh = d^2\sqrt{1 - (2\zeta - 1)^2}d\zeta. \tag{11}$$

By substituting Eqs. (3), (4), (6), (10), and (11) into Eq. (8), a nonlinear equation involving the unknown α for predetermined k and $m_1(= m - 1)$ can be derived:

$$\int_0^1 \left[(m_1\zeta^k + 1)(\zeta/\alpha - 1)\sqrt{1 - (2\zeta - 1)^2}|\zeta - \alpha|\right] d\zeta = 0, \tag{12}$$

when to solve for the unknown α, the trapezoidal rule (Burden et al., 2016) is employed for numerical integration of Eq. (12), while the bisection method (Burden et al., 2016), a numerical solution approach for nonlinear equations, is utilized to ascertain α.

As illustrative examples for the computation of the unknown α based on specific values of (k, m), **Fig. 3(a)** shows the curve of α versus k for selected values of $m = 0.5, 1$ and 2, while **Fig. 3(b)** depicts the curve of α versus m for $k = 0.5, 1$ and 2. In **Fig. 3(a)**, a homogeneous material characterized by $m = 1$ yields a constant $\alpha = 0.5$. For $m > 1$, α increases with rising k, peaks, and subsequently decreases; conversely, for $m < 1$, the opposite trend is observed. In Fig. 3(b), α consistently increases with increasing m, irrespective of k. For $m = 1$, all α values converge at $\alpha = 0.5$.

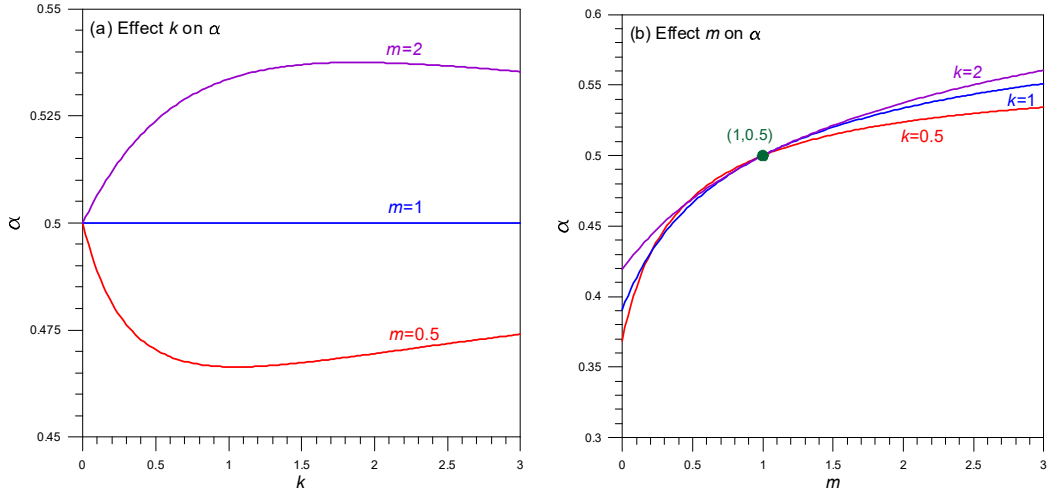

Fig. 3. (a) Curve of α - k for the selected m values; (b) Curve of α - m for the selected k values.

To visually represent the influence of (k, m) on α, **Fig. 4** presents a three-dimensional surface map illustrating the relationship among (α, k, m). This surface map effectively conveys the impact of (k, m) on α, as established in **Fig. 3(a)** and

Fig. 3(b).

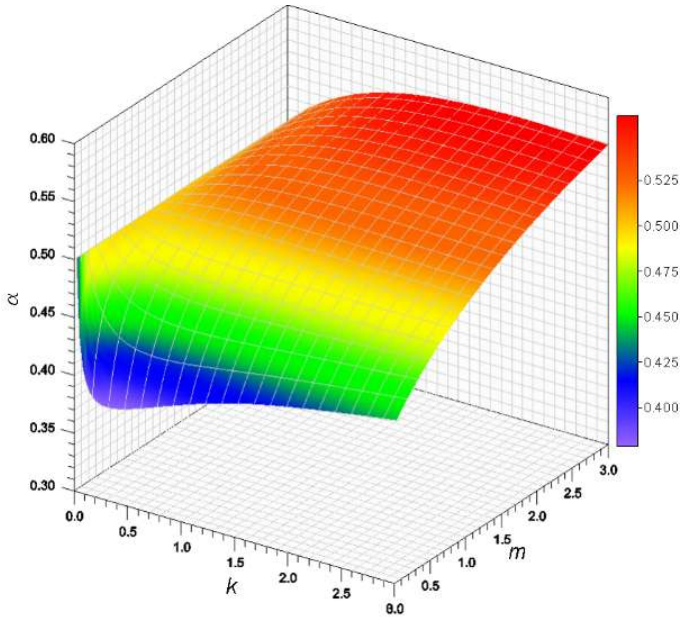

Fig. 4. Three-dimensional surface map of (α, k, m).

3.2. Generalized stiffness of LFGM

The primary objective of this study is to formulate four generalized stiffnesses: axial rigidity A_R, flexural rigidity F_R, mass per unit length D_m, and mass-moment of inertia I_m for the LFGM circular cross-section.

By definition, the axial rigidity A_R is the product of Young's modulus E and area A; thus, the infinitesimal axial rigidity dA_R of dA indicates the gray-shaded area depicted in **Fig. 1(a)**:

$$A_R = \int E dA = E_L d^2 \int_0^1 (m_1 \zeta^k + 1)\sqrt{1-(2\zeta-1)^2}\, d\zeta = \Psi E_L A, \tag{13a}$$

$$\Psi = \frac{4}{\pi}\int_0^1 (m_1 \zeta^k + 1)\sqrt{1-(2\zeta-1)^2}\, d\zeta, \tag{13b}$$

where $A = \pi d^2/4$ represents the area of the circular cross-section. For known material properties (k, m, E_L) and cross-sectional area A of the LFGM, A_R can be derived using Eq. (13). Importantly, the neutral position ratio α is not a factor in calculating Ψ, referred to hereafter as an area multiplier.

Flexural rigidity F_R is defined as the product of Young's modulus E and the second moment of area I. Hence, the infinitesimal dF_R of dA is represented as $dF_R = EdI$. The infinitesimal dI about the neutral axis $h = h_n$ can be expressed as:

$$dI = (h_n - h)^2 dA = d^4(\alpha - \zeta)^2\sqrt{1-(2\zeta-1)^2}\, d\zeta. \tag{14}$$

Consequently, F_R is computed as:

$$F_R = \int E dI = E_L d^4 \int_0^1 (m_1 \zeta^k + 1)(\alpha - \zeta)^2\sqrt{1-(2\zeta-1)^2}\, d\zeta = \Gamma E_L I, \tag{15a}$$

$$\Gamma = \frac{64}{\pi}\int_0^1 (m_1 \zeta^k + 1)(\alpha - \zeta)^2\sqrt{1-(2\zeta-1)^2}\, d\zeta, \tag{15b}$$

where $I = \pi d^4/64$ represents the moment of inertia of the circular cross-section. Based on known values (k, m, E_L, I) with previously determined α, Γ referred to as an inertia multiplier can be accordingly calculated.

In a similar process, the mass per unit length D_m, defined as the product of mass density ρ and the area A (Chopra, 2001), can be characterized as:

$$D_m = \int \rho dA = \rho_L d^2 \int_0^1 (m_1 \zeta^k + 1)\sqrt{1-(2\zeta-1)^2}\, d\zeta = \Psi \rho_L A, \tag{16}$$

with Ψ following from the equation already defined in Eq. (13b).

The mass-moment of inertia I_m, defined as the product of ρ and I (Chopra, 2001), is expressed as:

$$I_m = \int \rho dI = \rho_L d^4 \int_0^1 (m_1\zeta^k + 1)(\alpha - \zeta)^2 \sqrt{1-(2\zeta-1)^2}\, d\zeta = \Gamma \rho_L I, \tag{17}$$

where Γ is the same expression described in Eq. (15b).

To compute the multipliers (Ψ, Γ) expressed in Eqs. (13b) and (15b), respectively, the numerical integration methods (Burden et al., 2016) such as the Improved Euler method, Trapezoidal rule, and Runge-Kutta method may be employed. In this study, the Trapezoidal rule was chosen.

3.3. Numerical experiments of generalized stiffness

The previously defined multipliers (Ψ, Γ) for calculating the generalized stiffnesses (A_R, F_R, D_m, I_m) have been explicitly formulated in the preceding sections. As a numerical experiment, relationships depicting Ψ and Γ in relation to the exponential index k and the modular ratio m are illustrated in Fig. 5: (a) Ψ versus k curve, (b) Ψ versus m curve, (c) Γ versus k curve, and (d) Γ versus m curve. In **Fig. 5(a)**, at $m = 1$, corresponding to a homogeneous material, Ψ remains constant at $\Psi = 1$. For $m > 1$, Ψ decreases as k increases, while for $m < 1$, Ψ increases with rising k. In **Fig. 5(b)**, Ψ consistently shows growth with increasing k, independent of m. When $m = 1$, all instances yield $\Psi = 1$ as depicted earlier in Fig. 5(a). The Γ values in **Fig. 5(c)** and **Fig. 5(d)** exhibit similar trends to Ψ, although the Γ versus m curves in **Fig. 5(d)** reveal a nonlinear rather than linear relationship.

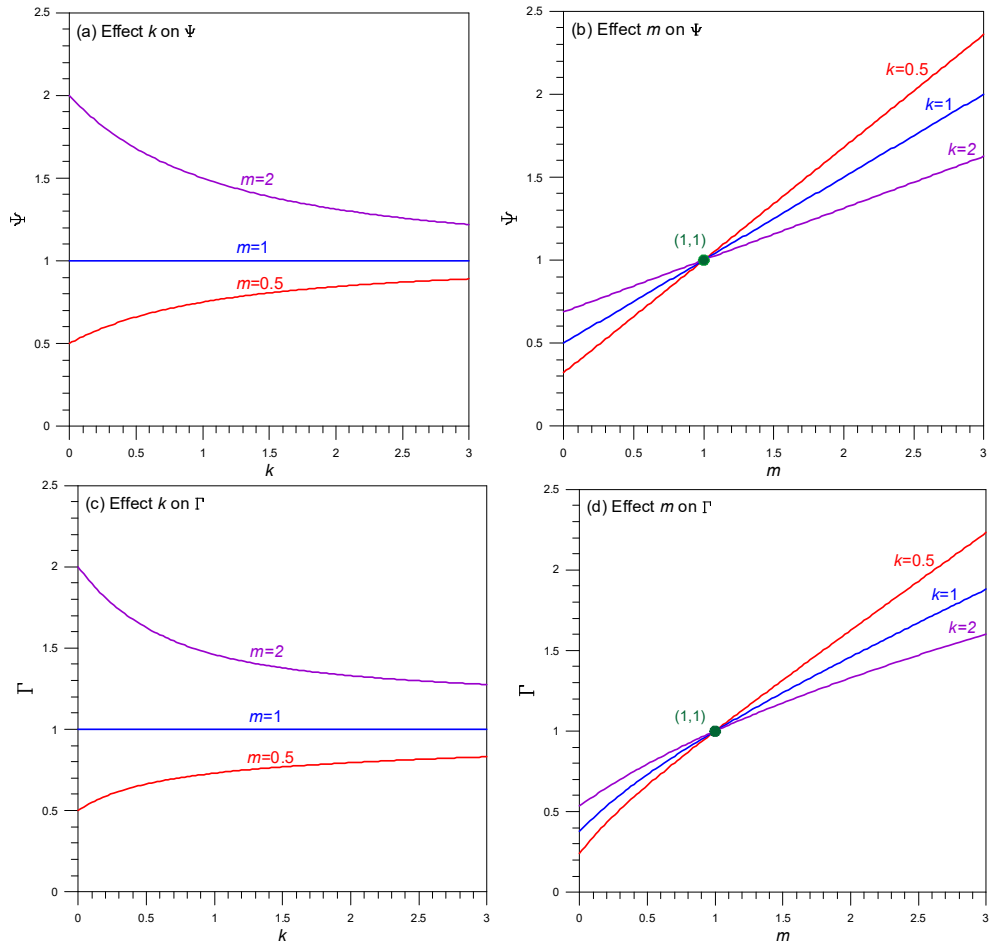

Fig. 5. (a) Ψ versus k curve, (b) Ψ versus m curve, (c) Γ versus k curve, and (d) Γ versus m curve

In order to visualize the effects of k and m on Ψ and Γ, three-dimensional surface maps are displayed in **Fig. 6: (a)** (Ψ, k, m) and (b) (Γ, k, m). These surface maps effectively illuminate the impact of (k, m) on (Ψ, Γ), reflecting observations made in **Fig. 5(a)** and **Fig. 5(b)**.

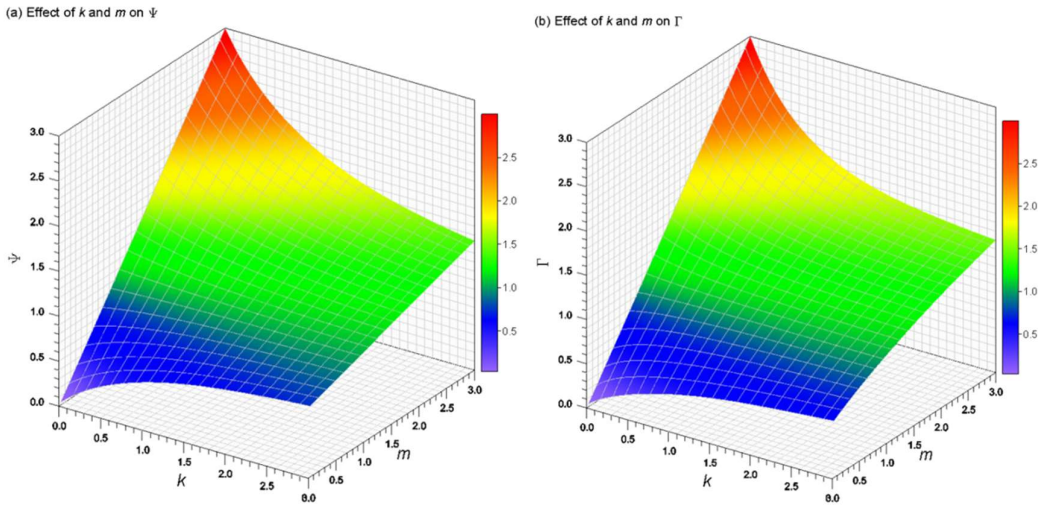

Fig. 6. Three-dimensional surface maps: (Ψ, k, m) and (b) (Γ, k, m)

As a numerical example, the dimensional generalized stiffnesses (A_R, F_R, D_m, I_m) for LFGMs, incorporating the neutral position h_n, are reported in **Table 1** based on the given values of (k, m). The circular cross-section features a diameter $d = 0.1$ m with an are $A = 7.854 \times 10^{-3}$ m² and moment of inertia $I = 4.909 \times 10^{-6}$ m⁴. The material properties of LFGM at $h = 0$ are specified as $\rho_L = 2700$ kg/m³ and $E_L = 70$ GPa. For each value of k, (A_R, F_R, D_m, I_m) increase as m increases; similarly, for each value of m, (A_R, F_R, D_m, I_m) rise as k increases. For $m = 1$, the quantities (A_R, F_R, D_m, I_m) remain constant irrespective of the k value. For instance, when $m = 1$, A_R equals $A_R = 549.8$ MN across all cases where $k = 0.5, 1$ and 2. A distinct advantage arising from the explicit calculation of generalized stiffness presented in this study is its direct applicability to structural analysis without the iterative internal calculations required by finite element methods.

Table 1. Dimensional generalized stiffness of LFGM* with varying (k, m)

Parameters		Dimensional generalized stiffness of LFGM				
k	m	h_n(m)	A_R(MN)	F_R(kN·m²)	D_m(kg/m)	I_m(kg·m)
0.5	0.5	0.04704	363.1	227.8	14.01	0.00879
	1	0.05	549.8	343.6	21.21	0.01325
	2	0.05239	923.1	558.4	35.61	0.02154
1	0.5	0.04664	412.3	250.8	15.90	0.00967
	1	0.05	549.8	346.3	21.21	0.01325
	2	0.05336	824.7	501.6	31.81	0.01935
2	0.5	0.04695	463.9	273.0	17.89	0.01053
	1	0.05	549.8	343.6	21.21	0.01325
	2	0.05374	721.6	456.8	27.83	0.01762

* Refer to the text for material and cross-sectional properties.

4. Application of generalized stiffness to dynamic beam element

The explicit formulation of generalized stiffness (A_R, F_R, D_m, I_m) derives potential applications within structural analysis. Various structural behavior topics, including bending analysis for static and dynamic applications, involve parameters such as deflection, strain/stress analysis, stability assessment, and natural frequency evaluation. Within this context, the free vibration of beams is addressed as a representative problem associated with generalized stiffness. However, the applicability of generalized stiffness is not limited to free vibrations and can extend to all structural behavior analyses involving static and dynamic beam elements.

4.1. Governing differential equation

To apply the coupled properties of (A_R, F_R, D_m, I_m), consideration is given to the free vibrations of beams, which exemplify typical problems related to these coupled properties. The straight dashed line in **Fig. 7** represents the undeformed static beam fabricated from LFGM, characterized by length l and defined by either hinged, fixed, or free ends. The beam features a circular cross-section with diameter d, while its coupled properties, including the neutral position h_n, have been previously established.

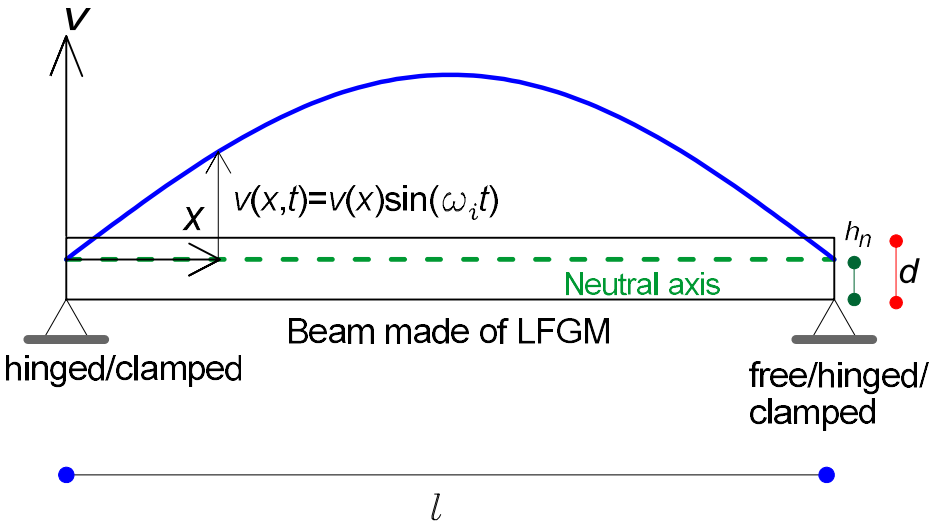

Fig. 7. Configuration of vibrating beam and its parameters

As the beam undergoes free vibration excitation, the dynamic transverse deflection is denoted by $v(x,t)$ in **Fig. 7**, where x is the axial coordinate and t signifies time. For this study, the transverse free vibration is assumed to exhibit harmonic motion, leading to the expression:

$$v(x,t) = v\sin(\omega_i t), \tag{18}$$

where $v = v(x)$ represents the amplitude at coordinate x, and ω_i denotes the natural frequency with integer mode number $i = 1, 2, 3, \cdots$.

The partial differential equation governing the transverse free vibration of the beam can be referenced from Chopra (2001):

$$\rho A\frac{\partial^2 v(x,t)}{\partial t^2} + EI\frac{\partial^4 v(x,t)}{\partial x^4} - \rho I\frac{\partial^4 v(x,t)}{\partial x^2 \partial t^2} = 0, \tag{19}$$

where $(\rho A, EI, \rho I)$ correspond to the mass per unit length, flexural rigidity, and mass-moment of inertia, respectively, applicable to homogeneous material beams. Notably, the three partial derivative terms with ρA, EI and ρI in Eq. (19) describe dynamic components representing bending moment, transverse inertia, and rotary inertia.

To adapt Eq. (19) for the LFGM beam, terms $(\rho A, EI, \rho I)$ are replaced with (D_m, F_R, I_m) of LFGM beams, resulting in the equation:

$$D_m\frac{\partial^2 v(x,t)}{\partial t^2} + F_R\frac{\partial^4 v(x,t)}{\partial x^4} - I_m\frac{\partial^4 v(x,t)}{\partial x^2 \partial t^2} = 0. \tag{20}$$

Applying Eq. (18), the relevant partial derivatives are derived as follows:

$$\frac{\partial^2 v(x,t)}{\partial t^2} = -\omega_i^2\sin(\omega_i t)\, v;\ \frac{\partial^4 v(x,t)}{\partial x^4} = \sin(\omega_i t)\frac{d^4 v}{dx^4};\ \frac{\partial^4 v(x,t)}{\partial x^2 \partial t^2} = -\omega_i^2\sin(\omega_i t)\frac{d^2 v}{dx^2}. \tag{21a–21c}$$

Substituting these relationships into Eq. (20) yields the ordinary differential equation governing transverse free vibration of the LFGM beam:

$$\frac{d^4 v}{dx^4} = -\frac{\rho_L}{E_L}\omega_i^2\left(\frac{d^2 v}{dx^2} - \frac{\Psi}{\Gamma}\frac{A}{I}v\right) \text{ for } 0 \le x \le l \tag{22}$$

To facilitate the numerical analysis within this study, the following dimensionless beam parameters are defined:

$$\xi = \frac{x}{l},\ \eta = \frac{v}{l},\ s = \frac{l}{\sqrt{I/A}},\ C_i = \omega_i l\sqrt{\frac{\rho_L}{E_L}}, \tag{23a–23d}$$

where, (ξ, η) depicts normalized coordinates, s represents slenderness, and C_i denotes the frequency parameter for integer mode number $i = 1, 2, 3, \cdots$.

Considering Eqs. (22) and (23), the governing non-dimensional differential equation can be expressed as:

$$\frac{d^4\eta}{d\xi^4} = -C_i^2\left(\frac{d^2\eta}{d\xi^2} - \frac{\Psi}{\Gamma}s^2\eta\right) \text{ for } 0 \le \xi \le 1 \tag{24}$$

Next, boundary conditions must be elucidated. At the hinged end ($x = 0$ or $x = l$), the deflection v and bending moment $M(= F_R\, d^2v/dx^2)$ are zero, leading to dimensionless conditions:

$$\text{Hinged end } (\xi = 0 \text{ or } \xi = 1):\ \eta = 0;\ \frac{d^2\eta}{d\xi^2} = 0. \tag{25}$$

At the clamped end ($x = 0$ or $x = l$), both v and rotation $\theta(= dv/dx)$ are zero, resulting in dimensionless forms:

$$\text{Clamped end } (\xi = 0 \text{ or } \xi = 1):\ \eta = 0;\ \frac{d\eta}{d\xi} = 0. \tag{26}$$

At the free end ($x = 0$ or $x = l$), both M and shear force $Q(= F_R\, d^3v/dx^3)$ equal zero, resulting in dimensionless conditions:

$$\text{Free end } (\xi = 0 \text{ or } \xi = 1):\ \frac{d^2\eta}{d\xi^2} = 0;\ \frac{d^3\eta}{d\xi^3} = 0. \tag{27}$$

4.2. Numerical solution method and validation

To solve the differential Eq. (24), beam parameters encompassing various end conditions such as hinged–hinged, hinged–clamped, clamped–clamped, and clamped–free must be defined, along with the beam length l, diameter d of circular cross-section, and material properties (k, m) and (ρ_L, E_L). Based on these parameters, (Ψ, Γ, s) can be computed and applied to Eq. (24). The numerical integration method, specifically the Runge-Kutta method (Burden et al., 2016), will then be utilized to compute $(\xi, \eta)_i$, adhering to the boundary conditions delineated by Eqs. (25)–(27).

The determinant search approach, combined with the bisection method, one of the nonlinear equation solution methods, is employed to identify the eigenvalue C_i. This method for initial and boundary value problem solutions featuring eigenvalues has been extensively utilized in existing literature (Lee and Lee, 2022), with comprehensive coding performed in the FORTRAN programming language to facilitate calculations for coupled properties (α, Ψ, Γ). Calculations are conducted on a PC equipped with graphical support.

The initial numerical experiment involves comparing natural frequencies ω_i obtained from the finite element method (FEM) with frequencies derived in this study to validate both the theoretical framework and numerical methods employed. The results are summarized in **Table 2**. Parameters used for the beam include $k = 2$, $l = 2$ m, $d = 0.1$ m with $A = 7.854 \times 10^{-3}$ m^2 and $I = 4.909 \times 10^{-6}$m^4, ($\rho_L = 2700$ kg/m^3, $E_L = 70$ GPa) at $h = 0$ and ($\rho_U = 5400$ kg/m^3, $E_U = 140$ GPa) at $h(= d) = 0.1$ m. This study derives a remaining parameter of modular ratio $m = 2$ alongside the slenderness ratio $s = 80(= l/\sqrt{I/A})$. The frequency parameter C_i, obtained through this study, translates to $\omega_i = 2545.9C_i$ rad/s using Eq. (23d). The ADINA software is employed to provide the FEM solution modeling the LFGM cross-section as 20 stepped-thick layers with varying material properties (ρ, E) characterized in Eq. (3). Comparisons of the first three natural frequencies $\omega_{i=1,2,3}$ in rad/s show strong agreement between the two methods, with an average error of 1.98% and a maximum error of 3.86%. The results presented in **Table 2** affirm the theoretical framework and numerical approaches undertaken, inclusive of coupled properties of LFGM used in this study.

Table 2. Comparison* of natural frequency ω_i between FEM** and this study

End constraint	Data source	Natural frequency ω_i (rad/s)		
		$i = 1$	$i = 2$	$i = 3$
Hinged-hinged	FEM	312.78	1243.21	2749.99
	This study	315.87	1260.54	2825.27
Hinged-clamped	FEM	489.26	1562.87	3221.22
	This study	493.39	1594.94	3314.42
Clamped-clamped	FEM	711.89	1921.97	3707.31
	This study	715.91	1968.18	3842.51
Clamped-free	FEM	111.10	698.20	1895.73
	This study	112.62	705.01	1968.99

* Refer to the text for beam parameters.
** ADINA

4.3. Numerical experiments

A parametric study investigating definitions of beam parameters (k, m, s) in relation to frequency parameters $C_{i=1,2,3}$ is presented in **Figs. 8(a)–8(b)**. **Fig. 8(a)** illustrates the moderate effect of exponential index k upon C_i, indicating negligible

variability. Conversely, **Fig. 8(b)** demonstrates that C_i escalates in response to increasing modular ratio m, though this effect becomes negligible for $m > 1$. Furthermore, **Fig. 8(c)** depicts a declining trend for C_i as slenderness ratio s increases, indicating enhanced sensitivity with smaller values of s.

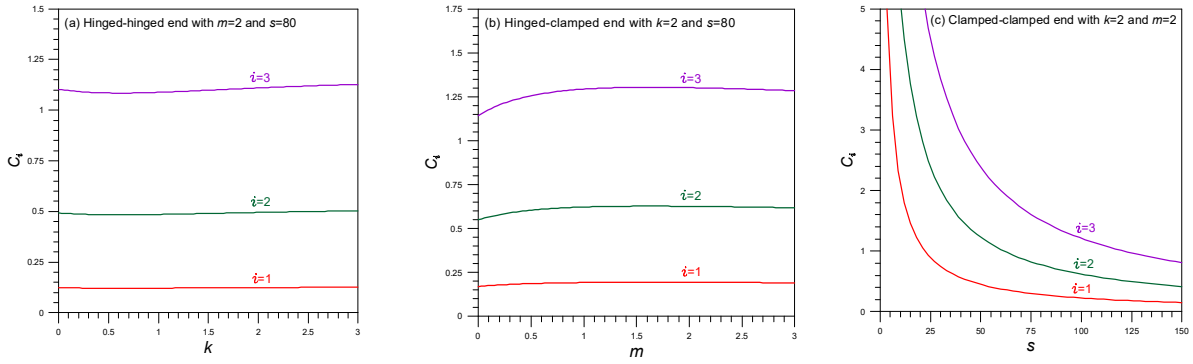

(a) (b) (c)

Fig. 8. Frequency curves of C_i as a function of (k, m, s): (a) Hinged–hinged for k, (b) Hinged–clamped for m, (c) Clamped–clamped for s.

Fig. 9 illustrates the effects of k and m on the lowest frequency parameter C_1 (i.e., $i = 1$) using surface maps, encapsulating the previously discussed frequency trends. The frequency curves demonstrated earlier are consolidated into a singular curve depicted in this surface map. The coupling of effects originating from (k, m) on C_1 is readily apparent from these surface maps.

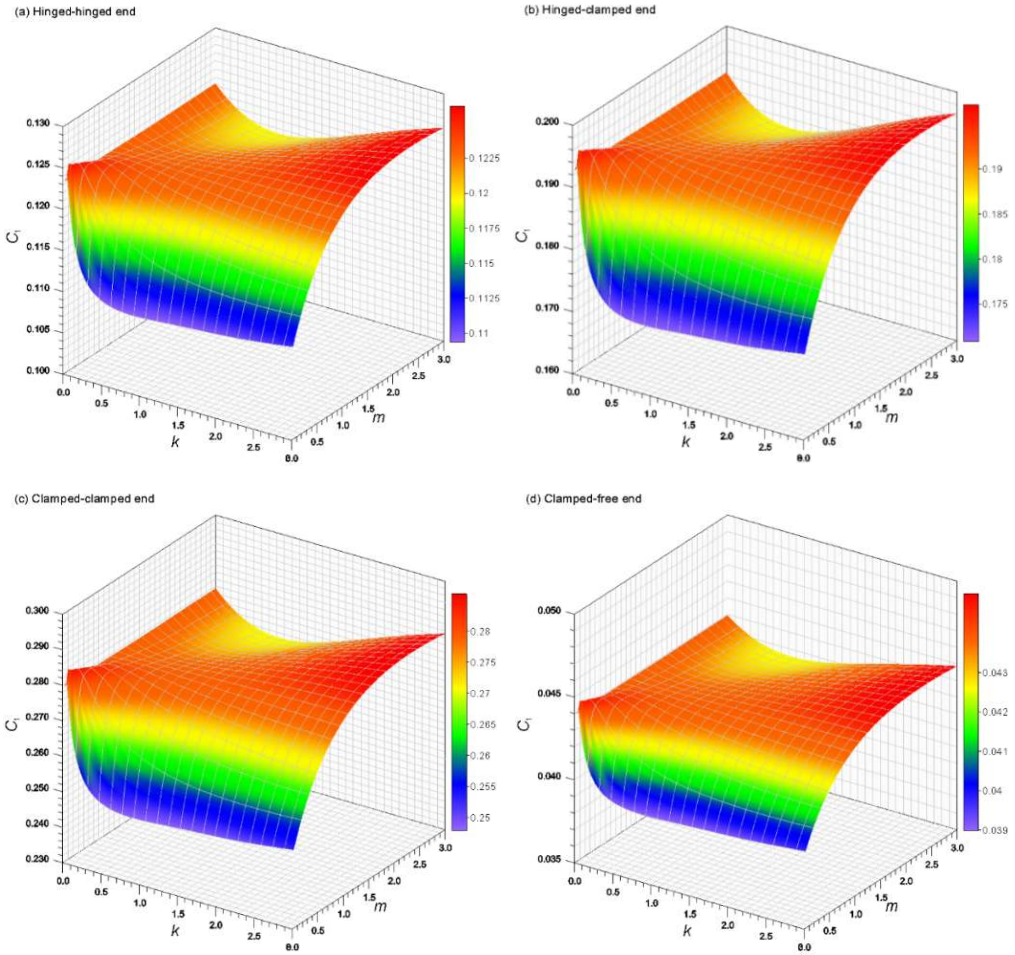

Fig. 9. Surface maps of (C_1, k, m) for $s = 80$: (a) Hinged–hinged, (b) Hinged–clamped, (c) Clamped–clamped and (d) Clamped–free end.

The typical mode shapes $(\xi, \eta)_i$ associated with corresponding C_i of the free-vibrating LFGM beam are exhibited in **Fig. 10**. The boundary conditions depicted by Eqs. (25)–(27) are effectively represented at both ends of the beam in the mode shapes demonstrated in **Fig. 10**. To mitigate resonance issues stemming from external dynamic excitation through mechanical devices, these mode shape outcomes furnish essential data for LFGM beam design, illustrating relative amplitude, peak amplitude positions, and locations of nodal points (where amplitude equals zero).

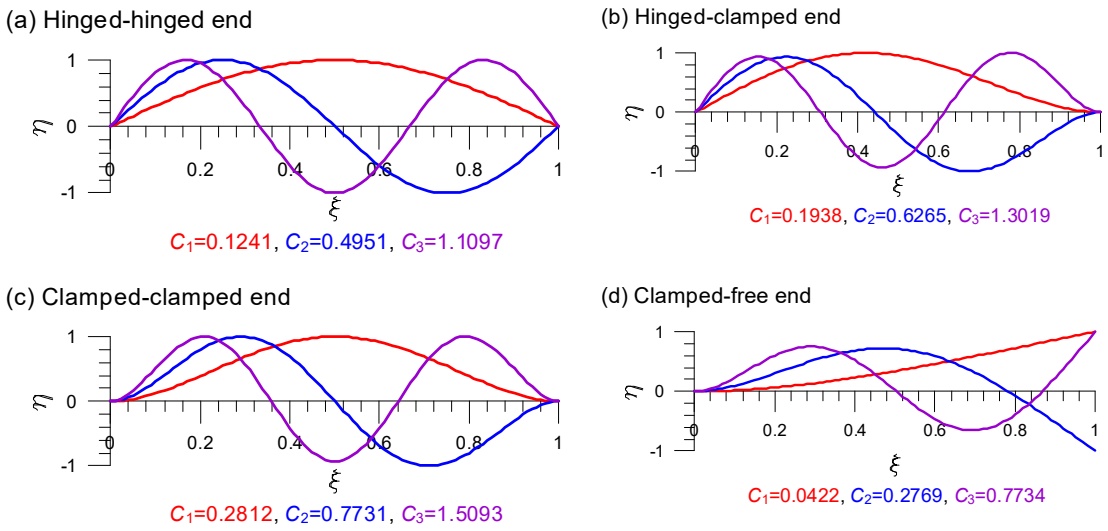

Fig. 10. Examples of mode shape for $k = 2$, $m = 2$, $s = 80$: (a) Hinged–hinged, (b) Hinged–clamped, (c) Clamped–clamped and (d) Clamped–free end.

5. Concluding remarks

This paper has investigated the generalized stiffness of laterally functionally graded materials (LFGMs) alongside its application to dynamic beam elements within the realm of structural mechanics. The primary focus of this study encompasses two key components.

Initially, the research formulates generalized stiffnesses for axial rigidity A_R, flexural rigidity F_R, mass per unit length D_m, and mass-moment of inertia I_m for the circular cross-section of LFGMs in an explicit manner. The material properties (ρ, E) are graded asymmetrically with respect to the centroidal axis of the circular cross-section, employing a power-law function for the graded profile. Numerical experiments yield results for coupled properties (A_R, F_R, D_m, I_m) presented through comprehensive tables and graphical charts reflecting a variety of modular ratios and exponential power indices.

In the subsequent portion of the research, relevant properties (F_R, D_m, I_m) derived from the principal formulation are applied to bending problems, specifically analyzing the free vibration phenomena in beams. An ordinary differential equation, inclusive of rotational inertia effects and associated boundary conditions, governs the free vibration dynamics of the LFGM beam, with the governing equation being numerically solved to extract eigenvalues (natural frequencies) and mode shapes. Strong correlations in natural frequencies between results derived from the finite element method and those originating from this study validate approach efficacy. Numerical investigations elucidate the relationships among natural frequencies and differing beam parameters.

The generalized stiffness established herein holds significant potential for broader applications beyond the free vibration of beams addressed in this study, including analyses of various structural behaviors characterized by static and dynamic beam elements. Further research endeavors should focus on exploiting generalized stiffness to examine additional structural behaviors, including strain/stress, deflection, and nonlinear behavior pertaining to both linear and curved beam structures.

References

Akgoz, B., & Civalek, O. (2013). Free vibration analysis of axially functionally graded Bernoulli-Euler microbeams based on the modified couple stress theory. *Composite Structures. 98,* 314–322. https://doi.org/10.1016/j.compstruct.2012.11.020

Alshorbagy, A.E., Eltaher, M.A., & Mahmoud, F.F. (2011). Free vibration characteristics of a functionally graded beam by finite element method. *Applied Mathematical Modelling. 35,* 412–425. https://doi.org/10.1016/j.apm.2010.07.006

Burden, R.L., Faires, D.J., & Burden, A.M. (2016). *Numerical analysis,* Boston, MA, USA: Cengage Learning.

Chopra, A.K. (2001). *Dynamics of structures,* Upper Saddle River, NJ, USA: Prentice-Hall, Inc.

Czechowski, L., & Kolakowski, Z. (2019). The study of buckling and post-buckling of a step-variable FGM box. *Materials. 12*(6), 918. https://doi.org/10.3390/ma12060918

Gere, J.M., & Timoshenko, S.P. (1980). *Mechanics of materials,* Boston, MA, USA: PWS Publishing Company.
Horibe, T.A., & Mori, K. (2015). Large deflections of tapered cantilever beams made of axially functionally graded materials. *Mechanical Engineering Journal. 5*(1)*,* 1–10. https://doi.org/10.1299/mej.17-00268
Huynh, T., Luu, A., & Lee, J. (2017). Bending, buckling and free vibration analyses of functionally graded curved beams with variable curvatures using isogeometric approach. *Meccanica. 52,* 2527–2546. https://doi.org/10.1007/s11012-016-0603-z
Javania, M., Kianib, Y., & Eslamia, M.R. (2019). Free vibration of arbitrary thick FGM deep arches using unconstrained higher-order shear deformation theory. *Thin-Walled Structures, 136,* 258–266. https://doi.org/10.1016/j.tws.2018.12.020
Kang, Y.A., & Li, X.F. (2009). Bending of functionally graded cantilever beam with power-law non-linearity subjected to an end force. *International Journal of Non-Linear Mechanics, 44*(6)*,* 696–703. https://doi.org/10.1016/j.ijnonlinmec.2009.02.016
Lee, J.K., & Lee, B.K. (2019). In-plane free vibration of uniform circular arches made of axially functionally graded materials. *International Journal of Structural Stability and Dynamics, 19*(7)*,* 1950084. https://doi.org/10.1142/S0219455419500846
Lee, J.K., & Lee, B.K. (2022a). Buckling optimization of axially functionally graded columns having constant volume. *Engineering Optimization, 542*(2), 269–285. https://doi.org/10.1080/0305215X.2020.1862824
Lee, J.K., & Lee, B.K. (2022b). Coupled flexural-torsional free vibration of an axially functionally graded circular curved beam. *Mechanics of Composite Materials, 57*(6)*,* 833–846. https://doi.org/10.1007/s11029-022-10003-8
Liu, Y., & Shu, D.W. (2014). Free vibration analysis of exponential functionally graded beams with a single delamination. *Composites Part: B-Engineering, 59,* 166–172. https://doi.org/10.1016/j.compositesb.2013.10.026
Malekzadeh, P. (2009). Two-dimensional in-plane free vibrations of functionally graded circular arches with temperature-dependent properties. *Composite Structures, 91*(1)*,* 38–47. https://doi.org/10.1016/j.compstruct.2009.04.034
Malekzadeh, P., Atashi, M.M., & Karami, G. (2009). In-plane free vibration of functionally graded circular arches with temperature-dependent properties under thermal environment. *Journal of Sound and Vibration. 326,* 837–851. https://doi.org/10.1016/j.jsv.2009.05.016
Noori, A.R., Aslan, T.A., & Temel, B. (2018). An efficient approach for in-plane free and forced vibrations of axially functionally graded parabolic arches with non-uniform cross section. *Composite Structures. 200,* 701–710. https://doi.org/10.1016/j.compstruct.2018.05.077
Qatu, M.S., & Elsharkawy, A.A. (1993). Vibration of laminated composite arches with deep curvature and arbitrary boundaries. *Computers & Structures. 47*(2)*,* 305–311. https://doi.org/10.1016/0045-7949(93)90381-M
Raki, M., Alipour, R., & Kamanbedast, A. (2012). Thermal buckling of thin rectangular FGM plate. *World Applied Science Journal, 16*(1)*,* 52–62.
Sitar, M., Kosel, F., & Brojan, M. (2014). Large deflections of nonlinearly elastic functionally graded composite beam. *Archives Civil and Mechanical Engineering, 14*(4)*,* 700–709. https://doi.org/10.1016/j.acme.2013.11.007
Trinh, T.H., Nguyen, D.K., Gan, B.S., & Alexandrov, A. (2016). Post-buckling responses of elastoplastic FGM beams on nonlinear elastic foundation. *Structural Engineering and Mechanics, 58*(3)*,* 515–532. https://doi.org/10.12989/sem.2016.58.3.515
Yousefi, A., & Rastgoo, A. (2011). Free vibration of functionally graded spatial curved beams. *Composite Structures. 93,* 3048–3056. https://doi.org/10.1016/j.compstruct.2011.04.024
Zaczynska, M., & Kazmierczyk, F. (2020). Multi-mode buckling analysis of FGM channel section beams. *Materials, 13*(11)*,* 2567. https://doi.org/10.3390/ma13112567
Zhao, F.Q., Wang, Z.M., & Zhang, R.P. (2012). Post-buckling analysis of FGM beam subjected to non-conservative forces and in-plane thermal loading. *Applied Mechanics and Materials. 152/154,* 474–479. https://doi.org/10.4028/www.scientific.net/AMM.152-154.474